Determination of ^{20}Ne(p,γ)^{21}Na cross sections from E_{p}=500−2000keV

S. Lyons, J. Görres, R. J. deBoer, E. Stech, Y. Chen, G. Gilardy, Q. Liu, A. M. Long, M. Moran, D. Robertson, C. Seymour, B. Vande Kolk, M. Wiescher, and A. Best

Phys. Rev. C **97**, 065802 — Published 5 June 2018

DOI: 10.1103/PhysRevC.97.065802

Determination of ^{20}Ne(p,γ)^{21}Na cross sections from E_p = 500 - 2000 keV

S. Lyons,* J. Görres, R.J. deBoer, E. Stech, Y. Chen, G. Gilardy, Q. Liu,
A.M. Long,† M. Moran, D. Robertson, C. Seymour, B. Vande Kolk, and M. Wiescher
Department of Physics, University of Notre Dame, Notre Dame, Indiana 46556, USA and
The Joint Institute for Nuclear Astrophysics, University of Notre Dame, Notre Dame, Indiana 46556, USA

A. Best
Dipartmento di Scienze Fisiche, Universitá Federico II and INFN Sezione di Napoli, Naples, Italy and
The Joint Institute for Nuclear Astrophysics, University of Notre Dame, Notre Dame, Indiana 46556, USA

Background: The reaction ^{20}Ne$(p,\gamma)^{21}$Na influences the nucleosynthesis of the Ne, Na, and Mg isotopes while contributing to hydrogen-burning in several stellar sites, such as red giants, asymptotic giant branch (AGB) stars, massive stars, and ONe novae. In the relevant temperature range for these environments (T = 0.05 - 0.5 GK), the main contributions to this reaction rate are from the direct capture process as well as the high-energy tail of a subthreshold resonance in the ground state transition at E_x = 2425 keV in the ^{21}Na compound nucleus.

Purpose: The previous measurement of this reaction reports cross sections with large uncertainties for the ground state transition. At higher energies, where the subthreshold resonance makes a smaller contribution to the total cross section, only upper limits are provided. This work aims to reduce the uncertainty in the cross section where direct capture dominates, as well as provide cross section data in previously unmeasured regions.

Method: The ^{20}Ne$(p,\gamma)^{21}$Na reaction was measured over a wide proton energy range (E_p = 0.5 - 2.0 MeV) at $\theta_{\rm lab} = 90^\circ$. Transitions to the ground state and to the 332 and 2425 keV excited states were observed. The primary transitions to these three bound states were utilized in an R-matrix analysis to determine the contributions of the direct capture and the subthreshold resonance to the total cross section.

Results: The cross sections of the present measurements have been found to be in good agreement with the previous data at low energy. Significantly improved cross section measurements have been obtained over the E_p = 1300 - 1900 keV region. The narrow resonance at $E_{\rm c.m.}$ = 1113 keV(E_x = 3544.3 keV) has also been remeasured and its strength has been found to be in good agreement with previous measurements.

Conclusions: An extrapolation of the S-factor of ^{20}Ne$(p,\gamma)^{21}$Na has been made to low energies using the R-matrix fit. The reaction rate from the subthreshold resonance was found to be the main contributor to the reaction rate at temperatures below about 0.1 GK. The present rate is lower in the temperature range of interest than those presented in current reaction rate libraries by up to 20%.

I. INTRODUCTION

In hydrogen burning shells of red giant stars, asymptotic giant branch (AGB) stars, novae, and in the cores of massive stars, proton capture may occur on ^{20}Ne nuclei. This reaction may proceed in these environments when temperatures are greater than T = 0.05 GK [1]. Astrophysical evidence for the NeNa cycle has been observed in red giant stars and novae [2–4]. The NeNa cycle synthesizes Ne, Na, and Mg isotopes through a series of proton captures and β-decays. The ^{20}Ne(p,γ)^{21}Na reaction is the first of the cycle and is assumed to have the slowest reaction rate [5], thereby determining the overall rate for the cycle. This rate therefore impacts the abundance of other nuclei in the NeNa cycle: ^{22}Na, a stellar γ-ray signature, and ^{22}Ne which, via the $^{22}Ne(\alpha$,n)^{25}Mg reaction, is an important neutron source for the s-process [6].

At low energies, the reaction rate of ^{20}Ne$(p,\gamma)^{21}$Na (Q = 2431.68 keV) has contributions from direct capture and a sub-threshold resonance as shown in Fig. 1. The high energy tail of the sub-threshold resonance dominates the reaction rate at $T \lesssim 0.1$ GK[7], with contributions from direct capture to the E = 2425 keV state. In an intermediate temperature range ($0.1 \lesssim T \lesssim 1$ GK) the direct capture to the E_x = 2425 keV excited state continues to contribute significantly, as individual resonances begin to dominate the reaction rate at temperatures as low as T = 0.4 GK[8]. At higher temperatures, above $T \approx 1$ GK, the E_x =3544.3 keV resonance is the main contributing component. In addition to this resonance, direct capture to E = 331.9 keV and 2425 keV along with higher-lying resonances make up significant contributions to the reaction rate.

The previous measurement of this cross section over the energy range from E_p = 0.3 - 2.1 MeV was performed by Rolfs *et al.* [7] using an extended gas target with natural Ne gas. Resultant cross sections were determined relative to the narrow resonance (Γ = 15.5(14) eV [9]) at $E_{c.m.}$ = 1113 keV using the resonance strength given by Thomas and Tanner [10]. From the cross sections, S-factors were calculated and extrapolated to low energies($E_p < 0.3$ MeV). Through this work, a contribu-

* Present address: National Superconducting Cyclotron Laboratory, Michigan State University, East Lansing, MI 48824, USA; lyons@nscl.msu.edu
† Present address: Physics Division, Los Alamos National Laboratory, Los Alamos, New Mexico 87545, USA

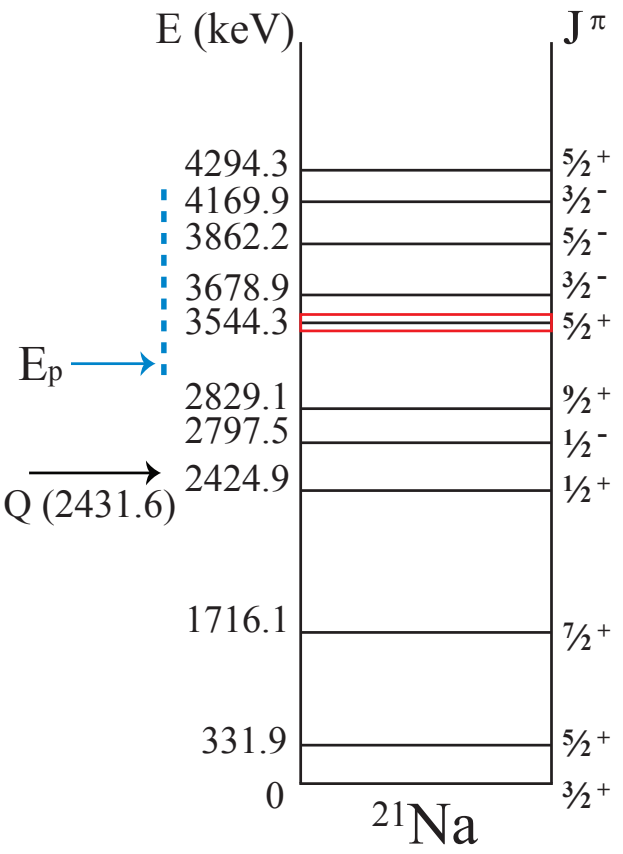

FIG. 1. Level diagram for ^{21}Na. Highlighted in red is the re-measured narrow resonance. The blue dashed line indicates the energy range (E_p = 0.5-2.0 MeV) of the cross section measurements that are discussed in Secs. III- IV. These measurements concentrate on the direct capture and broad resonance portions of the cross section that are pertinent for the extrapolation to stellar energies. It should be noted that the analysis of this work found the 4169.9 keV state to be at a significantly lower energy, which is discussed in Sec. IV.

tion from the high-energy tail of the sub-threshold resonance was identified. Uncertainties in this measurement motivated the present measurements.

In the present work, measurements of the cross section were made from E_p = 0.5 - 2.0 MeV using the St. ANA 5U-4 accelerator at the Nuclear Science Laboratory at the University of Notre Dame. A differentially pumped gas target of isotopically enriched ^{20}Ne was utilized. Cross sections were determined relative to the $E_{\rm c.m.}$ = 1113 keV resonance. The strength of this resonance was independently measured using a set of implanted targets. From the determined cross sections, astrophysical S-factors were calculated and extrapolated to the energy regions that correspond to stellar temperatures ($E_{\rm c.m.} < 500$ keV). Additionally, the rate was calculated and compared to those determined previously.

Sec. II provides a description of the experimental setup, procedure, and results for the strength measurements of the $E_{\rm c.m.}$ = 1113 keV resonance. In Sec. III, we discuss the cross section measurement, experimental setup, and procedures. Sec III B discusses the analysis and results from the cross section measurements. In Sec IV the level parameters from the R-matrix fits to the cross section data and the resultant extrapolated S-factors for the various transitions are discussed. Finally the reaction rate is presented in Sec. V along with comparisons to those found previously.

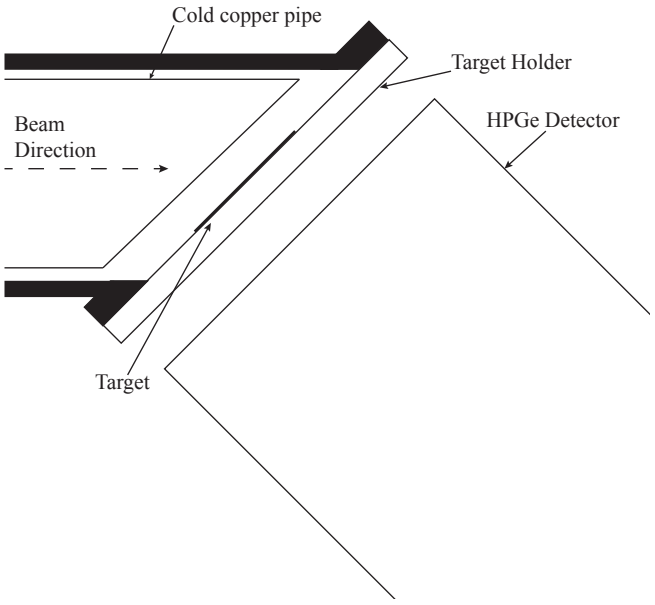

FIG. 2. Schematic of the experimental set-up used for measuring the strength of the ^{20}Ne$(p,\gamma)^{21}$Na resonance at $E_{\rm c.m.}$ = 1113 keV. Not to scale.

II. RESONANCE STRENGTH MEASUREMENT OF $E_{\rm c.m.}$ = 1113 KeV

A. Experimental Setup and Procedures

Strength measurements of the ^{20}Ne$(p,\gamma)^{21}$Na $E_{\rm c.m.}$ = 1113 keV resonance were performed with the KN accelerator at the Nuclear Science Laboratory at the University of Notre Dame. A 10 μA proton beam was impinged upon Ne implanted targets. Measurements were made using a 30% ORTEC HPGe detector, which was placed at 55° to the beam axis in order to reduce angular distribution effects. A schematic of the setup is shown in Fig. 2. Measurements at various distances from the target were made in order to determine summing effects.

The strength of a resonance is proportional to the integral of the cross section over the total width of the resonance [11], and can be calculated via,

$$\omega\gamma = \frac{2}{\lambda_R^2}\frac{1}{n}\frac{1}{B\eta W(\theta)}\int_0^\infty \frac{N(E_0)}{N_{beam}}dE_0, \qquad (1)$$

TABLE I. Implantation details for the various solid targets used. The targets are listed along with their respective backing material, the energy at which the implantation was performed, and the dose or accumulated charge from the implantation.

Target	Backing	Energy (keV)	Dose (mC)
^{20}Ne	Ta	150	200
Natural Ne	Ta	25	2430
^{22}Ne	Ta	150	80
^{22}Ne	Be	150	147

where λ_R^2 is the deBroglie wavelength at the resonance energy, n is the number of target nuclei, B is the branching ratio of the specific transition observed, η is the detection efficiency of the observed transition, and $W(\theta)$ is the angular distribution of the transition.

1. *Implanted Target Details*

A variety of both isotopically enriched targets of ^{20}Ne and ^{22}Ne, as well as a naturally enriched target were used to measure the $E_{\rm c.m.} = 1113$ keV resonance in ^{20}Ne$(p,\gamma)^{21}$Na and the $E_{\rm c.m.} = 1222$ keV resonance in ^{22}Ne$(p,\gamma)^{23}$Na. Table I details the implantation dose and backing material used for each of the targets. Information on the implantation of the targets is summarized in Table I.

The targets were analyzed using Rutherford Backscattering (RBS), which was used to characterize the number of target nuclei. The results of the RBS analysis were found to be consistent with TRIM calculations to within 8%. The beryllium target implanted with ^{22}Ne was used as a reference when determining the number of target nuclei in the other targets due to the well separated peaks of Be and ^{22}Ne in the RBS spectra. The number of neon nuclei in the other targets was then determined by comparing the yields of measured resonances. Using the enriched ^{22}Ne implanted Be target, yields from the $E_{\rm c.m} = 1222$ keV resonance in ^{22}Ne$(p,\gamma)^{23}$Na were determined and directly compared to the same resonance yield measured from the natural Ne implanted Ta target. With this comparison, along with the known abundance ratios, the amount of ^{20}Ne in the natural Ne implanted target was determined. The determined amount of ^{20}Ne in the natural implanted target was then used to find the number of nuclei in the enriched ^{20}Ne target by comparing yields from the $E_{\rm c.m} = 1113$ keV ^{20}Ne$(p,\gamma)^{21}$Na resonance in both targets. The target characterization is summarized in Table II.

2. *Efficiency*

The absolute peak efficiency for the ORTEC HPGe detector was determined using ^{56}Co and ^{60}Co calibrated sources, as well as three known resonances in ^{27}Al$(p,\gamma)^{28}$Si: 992, 1317, and 1780 keV [12, 13]. The resonances provided efficiency information from $E_\gamma = 1.5$ - 12 MeV, which was required to characterize the detector for the observation of the ground state transition in ^{22}Ne$(p,\gamma)^{23}$Na ($Q = 8794$ keV) resonance at $E_{\rm c.m.} = 1222$ keV. The data were then fit with the following functional form [14]

$$\ln(\varepsilon_{fe}) = a + b\ln(E_\gamma) + c\ln(E_\gamma)^2. \qquad (2)$$

GEANT4 [15] simulations of the experimental setup were performed and were found to be consistent with the present measurements as shown in Fig. 3

TABLE II. Characterization of the implanted targets as determined through the measured resonance yields as described in the text.

Target	Backing	Res. Yield (arb. units)	# Target Nuclei (at/cm^2)
^{20}Ne	Ta	$6.62(15)\times10^{-12}$	$5.52(56)\times10^{17}$
^{20}Ne (Nat.)	Ta	$6.44(49)\times10^{-13}$	$5.36(22)\times10^{16}$
^{22}Ne (Nat.)	Ta	$6.58(50)\times10^{-14}$	$5.49(22)\times10^{15}$
^{22}Ne	Ta	$2.30(9)\times10^{-12}$	$1.92(9)\times10^{17}$
^{22}Ne	Be	$3.93(10)\times10^{-12}$	[a]$3.28(9)\times10^{17}$

[a] Measured with Rutherford Backscattering.

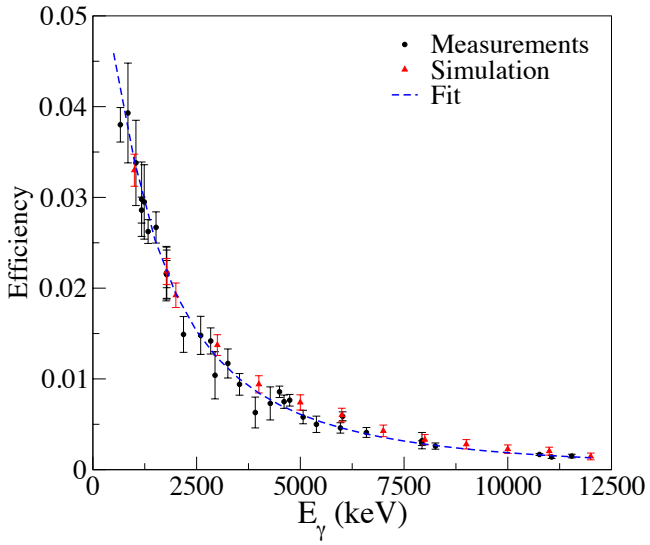

FIG. 3. (Color online) Absolute efficiency as a function of γ-ray energy. The black diamonds show results from the various measurements, the red triangles are simulation results from GEANT4, and the blue line is the fit to the data.

B. Analysis and Results

Using the isotopically enriched ^{20}Ne targets, primary and secondary transitions were observed in the resonance at $E_{\rm c.m.} = 1113$ keV. The strength for this resonance

TABLE III. A summary of $E_{c.m.}$=1113 keV resonance strengths. Previous literature values along with the present value are presented. The weighted average of all values was determined as the adopted value.

Thomas and Tanner [10]	0.98 ± 0.06
Keinonen *et al.* [18]	0.79 ± 0.15
Engel *et al.* [19]	0.84 ± 0.10
Christian *et al.* [17]	0.97 ± 0.11
Present Work	0.96 ± 0.10
Adopted	0.94 ± 0.04

was then calculated using the thick target yields from these transitions. Summing corrections were necessary for determining the resonance strength and were deduced by measuring the yield at several distances from the target for the same incoming proton energy [16]. The present value of 0.96 ± 0.10 eV was determined by taking the weighted average of the dominant R→GS transition, R→1716 transition, and the secondary 1716→GS transition.

As can be seen from the results presented in Table III, the adopted resonance strength is in agreement with the previous values. It was shown by Christian *et al.* [17], that the results of the Thomas and Tanner [10] measurement were initially presented in the laboratory reference frame, requiring a conversion to the center-of-mass frame to compare them with the other measurements of the resonance strength. The present results are in excellent agreement with both the corrected Thomas and Tanner [10] and Christian *et al.* [17] values. A weighted average of previous literature values as well as the value determined in this work was used to determine the adopted value, 0.94 ± 0.04 eV, of this resonance strength.

III. THE ^{20}Ne$(p,\gamma)^{21}$Na CROSS SECTION

In this work, the ^{20}Ne$(p,\gamma)^{21}$Na cross section was determined over a wide energy range, E_p = 0.5 - 2.0 MeV, relative to the $E_{\rm c.m.}$ = 1113 keV resonance. Particular focus was given to measuring the transition R/DC→GS.

A. Experimental Setup and Procedure

The measurement of ^{20}Ne$(p,\gamma)^{21}$Na was one of the first experiments performed with the University of Notre Dame's St. ANA 5U Accelerator. The accelerator is a 5 MV pelletron equipped with an ECR source in the terminal, which supplies a wide range of both beam species and intensities. Prior to the experiment, the energy defining analyzing magnet was calibrated using several known resonances in ^{27}Al$(p,\gamma)^{28}$Si and a typical energy resolution of 0.3 keV was determined. For this experiment, proton beam intensities of 10 - 50 μA were used.

The measurements were performed using Rhinoceros, a differentially pumped gas target system[20], in extended gas target mode. The so-called "Octopus" chamber was used as the target chamber. The chamber is a flat disk chamber with several ports at various angles. The gas target was operated with 4 Torr of ^{20}Ne enriched gas, resulting in a target thickness of ≈10 keV at $E_{\rm c.m.}$ = 1113 MeV.

A Canberra HPGe detector(100%) was placed at 90°, with respect to the beam, facing the target area. Measurements were made at various distances from the face of the target in order to determine summing corrections. A representative γ-ray spectra is shown in Fig.4. A 6.5 mm thick lead absorber was placed in front of the detector for the higher energy measurements in order to shield against the low-energy γ-rays, thus reducing the detector deadtime as well as summing. Additional lead shielding, as shown in Fig. 5, was placed around the face of the detector in order to reduce beam induced background from the beam dump and upstream collimators, which define the pumping regions in Rhinoceros [20].

The Octopus chamber was configured with a gas inlet on the 75° port. A baratron, used to monitor the target pressure to within 0.01 Torr, was placed on the 90° port. Because standard charge integration methods could not be used to determine total number of beam particles, Rutherford scattering, measured by two ruggedized Si detectors at 135° and 160°, was used for normalization. The Si detectors were collimated using a slit (0.5 mm) and hole (r = 0.762 mm) separated by a distance of 25 mm.

1. *Efficiency*

To determine the peak efficiency of the detector, several calibrated sources were measured from the center of the target chamber. The calibrated sources used were ^{137}Cs, ^{60}Co, and ^{56}Co. A ^{66}Ga source was created via activation in order to measure the efficiency up to E_γ = 4.8 MeV. Due to the use of the Pb absorber during measurements made above E_p = 1.3 MeV, the peak efficiency was determined independently for both set-ups. Fig. 6 shows the peak efficiency curves as a function of γ-ray energy determined for both cases. GEANT4 simulations of the experimental set-up were performed and are in excellent agreement with the data. The peak efficiency was also measured with respect to the distance from the target face. Measurements made at 10 cm from the target reduced the peak efficiency by as much as 80% compared to the running position.

The efficiency was also measured as a function of position within the extended target using known sources. Measurements every 10 mm along the beam axis in the target chamber were performed for both the close distance (6.5 mm from target face) and far distance (10 cm from target face). Fig. 7 shows the efficiency as a function of position along the beam axis in the target chamber. Again, GEANT4 simulations were performed and are in agreement with the data for both distance geometries.

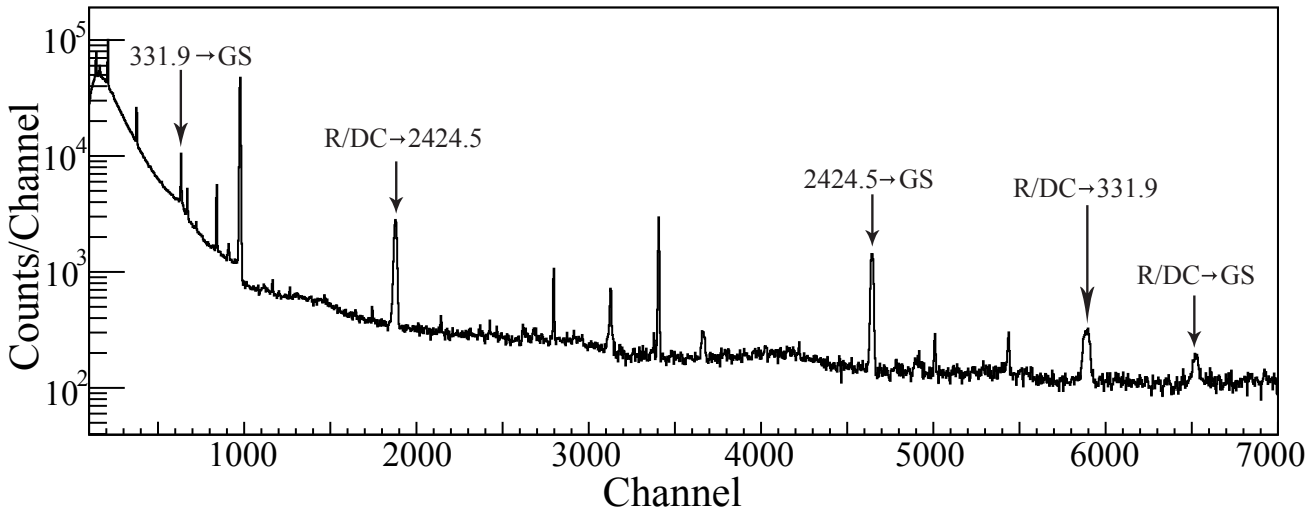

FIG. 4. Representative γ-ray spectrum from measurement made at E_p = 1030 keV. The observed primary and secondary transitions from the ^{20}Ne$(p,\gamma)^{21}$Na reaction are labeled.

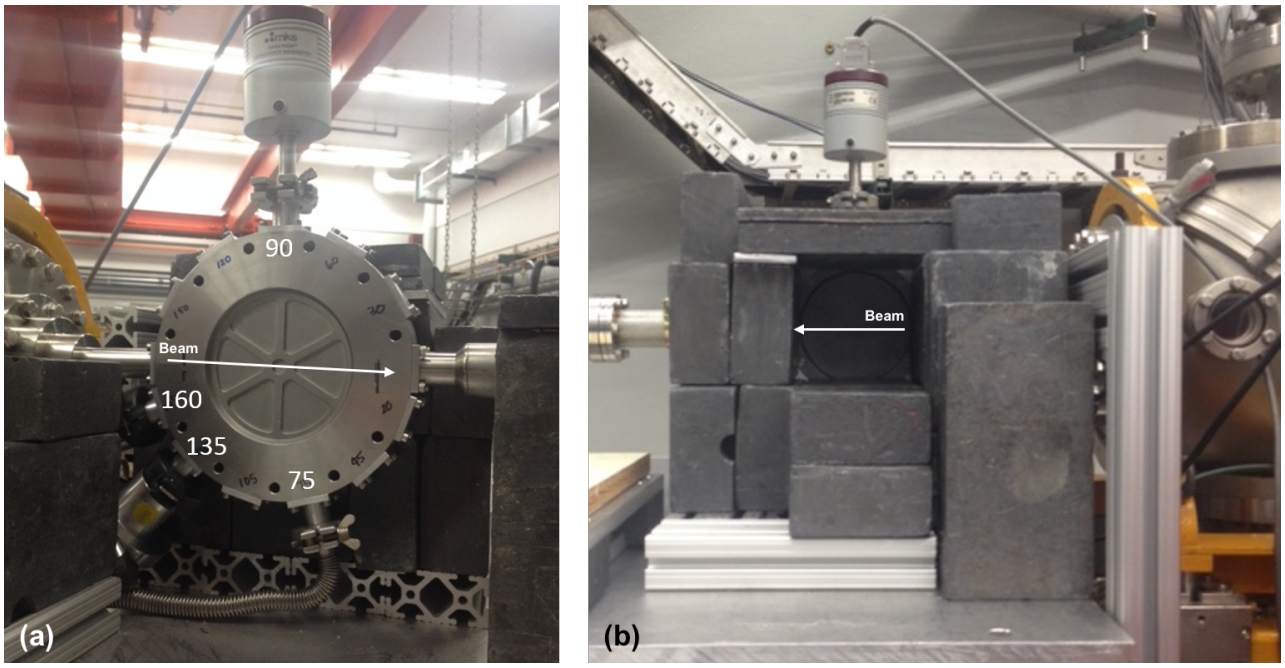

FIG. 5. (Color online) Experimental set-up for cross section measurements. (a) The Octopus chamber set up with the angles of various ports labeled as observed from beam right. (b) The lead shielding around the detector area that was used to reduce the beam-induced background and further define the target area as observed from beam left.

The shapes of the efficiencies as a function of position within the target chamber are different for each of the distances due to changes in the solid angle viewed by the detector. At close distance, the shape is Gaussian, while at far distance the shape is arctangent in nature and the efficiency is uniform across the central part of the target area.

2. *Rutherford Scattering*

As previously mentioned, elastic scattering was used to normalize the data for the cross section determination. From Rolfs *et al.* [7], it was known that at higher energies, the scattering deviates from Rutherford. To correct for this effect, measurements of the elastic scattering from E_p = 1.6 - 2.0 MeV were performed with ^{20}Ne and natural Xe gas in a ratio of 8:1. Measurements

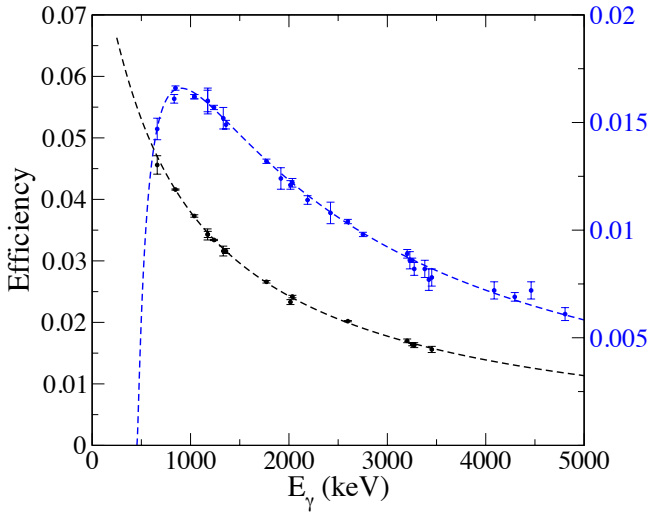

FIG. 6. (Color online) Efficiency both without (black) and with (blue) the Pb absorber. The dashed lines are the corresponding fits to the data using Eq.2. The right vertical axis corresponds to the scaling for the data with the Pb absorber. The effects of the Pb absorber cause an overall reduction in the efficiency, as well as to the low-energy efficiency.

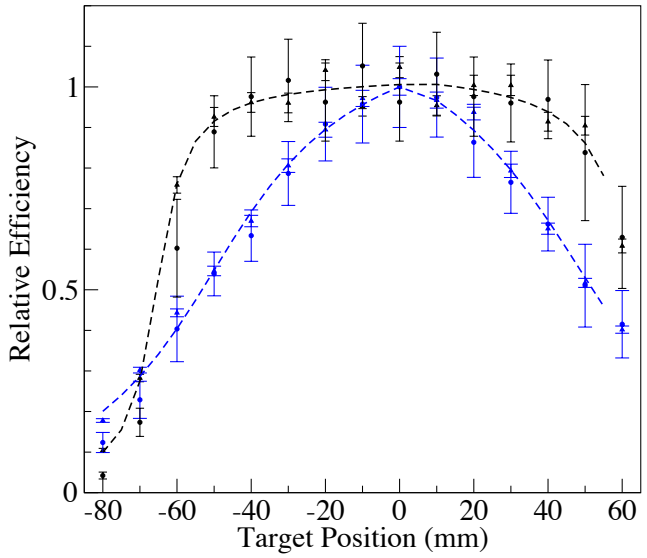

FIG. 7. (Color online) Efficiency as a function of position within the target, comparing both the detector in close distance geometry (blue data) and far distance geometry (black data). GEANT4 simulations were performed and included in data shown. The results are in agreement with the measurements. The dashed lines correspond to best fits for each shape, arctangent in black and Gaussian in blue. The beam enters at the target chamber at the 60 mm point with center at 0 mm and the exit at -60 mm. Further distances towards the beamstop were measured to understand the full effects of the Pb shielding.

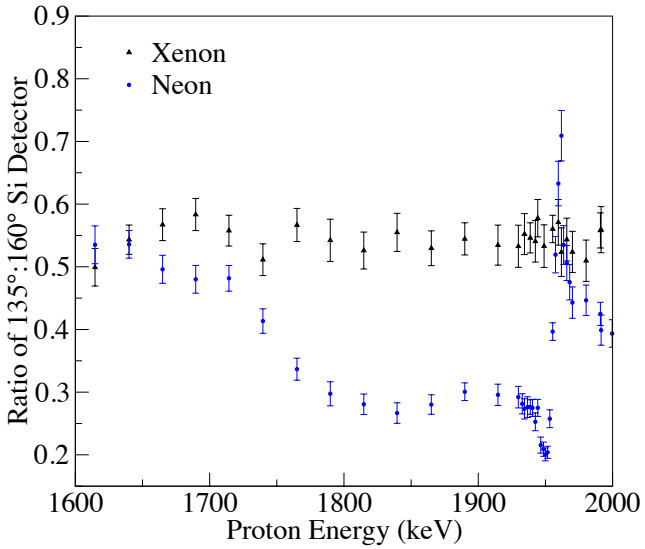

FIG. 8. (Color online) Proton scattering measurements for Ne and Xe. The scattering deviates from Rutherford at $E_p \geq$ 1600 keV in Ne. Using the Xe scattering, corrections to the experimental normalization were deduced.

were taken at 135° and 160°, and then a ratio between the two detectors was compared. The resultant ratio for both Xe and Ne is shown in Fig. 8. The difference in the ratio between Xe and Ne was used to determine the necessary corrections for normalization.

3. *Angular Distributions*

The cross sections in this work were determined relative to the strong narrow resonance at $E_{\rm c.m.}$= 1113 keV (see Sec. III B, Eq. (6)). This procedure requires that the angular distributions for both this narrow resonance and that of the slowly varying portion of the cross section be be taken into account. The angular distributions can be written in the form

$$W(\theta) = \sum_{0}^{n} a_n Q_n P_n(\cos(\theta)), \qquad (3)$$

where the a_n are the angular distribution coefficients, the Q_n are the angular attenuation coefficients, P_n are the Legendre polynomials, and θ defines the angle of the detector relative to the beam direction. Because of the limitations of the extended gas target setup, these angular distributions could not be measured and instead were calculated from theory.

For the narrow resonance at $E_{\rm c.m.}$= 1113 keV, the corresponding state in ^{21}Na is well known and has a spin-parity of $J = 5/2^+$ [21–23]. The ground state transition angular distribution has been measured experimentally by Van der Leun and Mouton [22] and is compared to theoretically calculated angular distributions in Fig. 9a. The slowly varying portions of the cross section observed

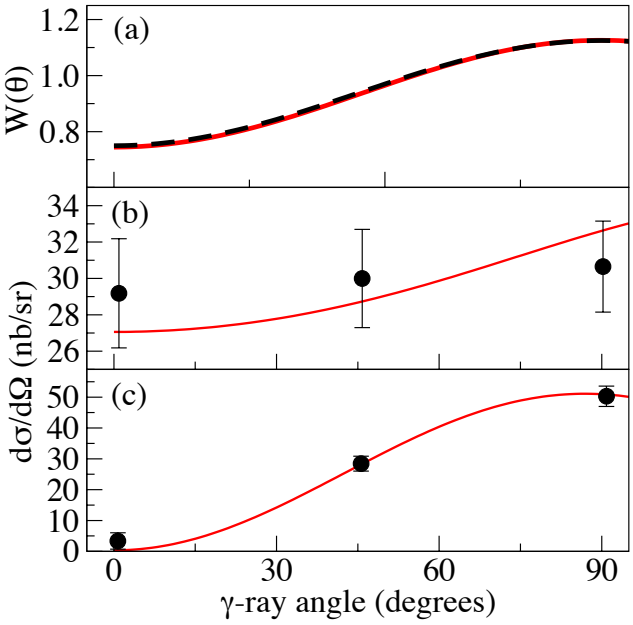

FIG. 9. (Color online) a) Theoretical angular distributions for the $E_{c.m.}$= 1113 keV resonance (red line) calculated with AZURE2 (using a multipole mixing ratio of $\delta_{E2/M1}$ = 0.07±0.02 [22]) compared to the measured distribution (reported as angular distribution coefficients) in Van der Leun and Mouton [22] (black dashed line). Angular distributions from Rolfs *et al.* [7] (black data) compared to the cross section arising from the external capture model using AZURE2 (red line) for the DC→332 keV transition, b), and the DC→2425 keV transition, c).

at $\theta = 90°$ can be described well by the external capture model. The only angular distribution data available for the off-resonance regions are the relative intensities given in Figs. 6 and 7 of Rolfs *et al.* [7]. Fig. 9 shows a comparison of the angular distributions found in the literature compared to the theoretical calculations used for this work.

These theoretically calculated angular distributions were used to calculate the angular distribution coefficients, a_n, given in Table IV.

The angular attenuation coefficients [24],

$$Q_n = \frac{\int_0^{\beta_{max}} P_n(\cos(\beta))\eta(\beta, E)\sin\beta d\beta}{\int_0^{\beta_{max}} \eta(\beta, E)\sin\beta d\beta}, \qquad (4)$$

were calculated using a GEANT4 simulation. These angular attenuation coefficients are dependent on the geometry and efficency of detector. Here β is the angle between where the radiation hits the detector and the detector symmetry axis, and $\eta(\beta, E)$ is the peak efficiency for the radiation of energy E at angle β. At low energies, penetrability ensures that only the lowest few angular momentum terms will be significant. Further, at 90° where the present measurements were made, the odd order Legendre polynomials vanish, therefore only $n = 2$ and 4 terms were considered. Angular attenuation coefficients of $Q_2 = 0.69 \pm 0.03$ and $Q_4 = 0.26 \pm 0.05$ were determined for the close geometry and $Q_2 = 0.96 \pm 0.01$ and $Q_4 = 0.88 \pm 0.01$ were determined for the far geometry.

TABLE IV. Angular distribution coefficients. The a_n parameters determined using AZURE2 [25]. Values for Q_2 and Q_4 were determined to be 0.69(3) and 0.26(5), respectively, using a GEANT4 simulation.

Transition	a_2	a_4	$W(90°)$
R (1113 keV) → 0	-0.250	0	1.086
R/DC → 0	0.010	1.75×10^{-4}	0.996
R/DC → 332	0.092	1.43×10^{-3}	0.968
R/DC → 2425	-0.997	-3.09×10^{-3}	1.346

4. *Summing Corrections*

Summing corrections were determined for both the $E_{c.m} = 1113$ keV resonance and the low-energy cross section data. To obtain the summing corrections experimentally, measurements were made in close(6.5 mm from target face) and far(10 cm from the target face) geometry at the same incoming proton energy. It was found that a distance of 10 cm from the target face was sufficient to provide negligible summing contributions compared to the statistical uncertainties of the reaction yields and this distance was used as the far position. It was determined for the ground state transition in the $E_{c.m} = 1113$ keV resonance that no summing correction was necessary, which stems from this transition being the dominant transition with a branching ratio of 92%.

The summing effects for the low-energy data were obtained using direct capture measurements at $E_p = 1130$ keV. Correction factors (CF in Table V) were determined by taking a ratio between close and far distance yield normalized to the R/DC→332 yield which is known to be isotropic. GEANT4 simulations were performed and compared to the measurements. The simulated corrections were found to be within 10% of the measured correction factors as shown in Table V, with the exception of the correction factor for the R/DC→GS component. The R/DC→GS component simulations produced a correction factor that is 30% lower than the measured value. This is due to difficulties integrating the subthreshold resonance and it's contributions into the simulation because the ratio between the subthreshold resonance and the direct capture component of the reaction are unknown. Additionally, it should be also noted that the R/DC→GS transition is very weak, so summing-in effects can contribute a significant fraction of the observed yield at the close distance of the current setup. The correction factors were folded into the experimental yields when deducing cross sections.

TABLE V. Direct Capture Summing Corrections. The correction factor (CF) is derived from comparing the close and far distance yield ratios for the various transitions.

Transition	$\left(\frac{Y_{Trans}}{Y_{\sigma\to 332}}\right)_{close}$	$\left(\frac{Y_{Trans}}{Y_{\sigma\to 332}}\right)_{far}$	$\mathrm{CF}_{meas.}$	CF_{Geant}
R/DC→GS	0.18	0.12	0.66	0.44
R/DC→2425	4.53	6.21	1.37	1.25
2425→GS	2.43	2.64	1.09	1.03
332→GS	298.26	375.42	1.26	1.20

B. Analysis and Results

Gamma-rays from the primary and secondary transitions in $^{20}\mathrm{Ne}(p,\gamma)^{21}\mathrm{Na}$ were observed during the experiment. These transitions were analyzed and cross sections determined relative to the $E_{\mathrm{c.m.}} = 1113$ keV resonance, which has been independently measured (Sec. II). The strongest transition (R→GS) from the $E_{\mathrm{c.m.}} = 1113$ keV resonance was used to determine the cross sections. This was done using the method described by Rolfs *et al.* [7] where

$$\sigma_{R/DC} = \frac{\lambda_r^2}{2}\frac{m+M}{m}\frac{\omega\gamma}{\Delta E}\frac{Y_{R/DC}}{Y_{1113}} \tag{5}$$

and

$$\frac{Y_{R/DC}}{Y_{1113}} = \frac{N_{R/DC}}{N_{1113}}\frac{\epsilon_{1113}}{\epsilon_{R/DC}}\frac{\Omega_{1113}}{\Omega_{R/DC}}\frac{W(\theta)_{1113}}{W(\theta)_{R/DC}}. \tag{6}$$

Here "R/DC" stands for data from direct capture as well as resonance interference, while "1113" denotes the parameters from the $E_{\mathrm{c.m.}} = 1113$ keV resonance. The parameters used are the projectile and target masses, m and M, respectively, ΔE is the target thickness, and $Y_{R/DC}/Y_{1113}$ is the yield ratio. The yield ratio is determined by the counts ($N_{R/DC}/N_{1113}$), the stopping powers ($\epsilon_{DC}/\epsilon_{1113}$), solid angle ($\Omega_{R/DC}/\Omega_{1113}$), and angular distributions ($W(\theta)_{R/DC}/W(\theta)_{1113}$). The $N_{R/DC}/N_{1113}$ are the branching ratio and efficiency corrected counts from the spectra. The cross section measurements were normalized to Rutherford scattering by:

$$N_{\mathrm{beam}} = \frac{\frac{N}{n\Omega}}{\left[\frac{d\sigma(E)}{d\Omega}\right]_\theta^{Ruth}}. \tag{7}$$

This equation includes the correction for any deviation from Rutherford. The cross sections from the various transitions were compared to Rolfs *et al.* [7]. Because Rolfs *et al.* [7] used the original resonance strength given by Thomas and Tanner [10], the cross sections were first corrected to reflect the center-of-mass Thomas and Tanner resonance strength value, 0.975 ± 0.06 (see Sec. II B). All of the transitions presented in Rolfs *et al.* [7] were observed in the present measurement, allowing for comparison of all transitions. The data contains 10% systematic error due to target thickness and efficiency.

Fig. 10 shows the R/DC→GS cross sections. The present low-energy cross sections are consistent with Stech [26] and within error of Rolfs *et al.* [7]. The most significant improvements to the R/DC→GS cross section are in the E_p = 1.3 - 2.0 MeV region, where only upper limits were previously available in Rolfs *et al.* [7]. The present measurements are in agreement with the upper limits of that work.

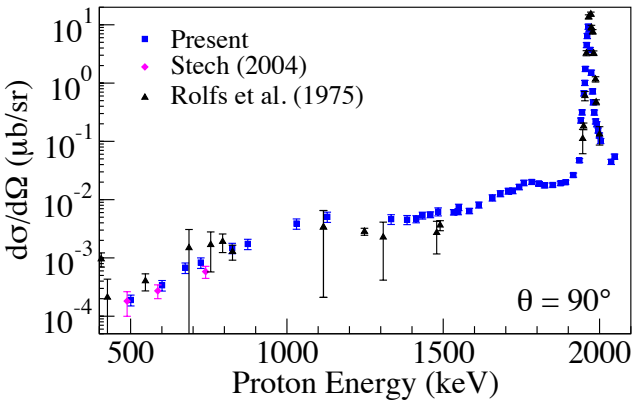

FIG. 10. (Color online) R/DC to ground state cross sections of the present work (blue) compared to Rolfs *et al.* [7] (black) and Stech [26] (pink). The narrow resonance at $E_{\mathrm{c.m.}} = 1113$ keV was intentionally removed for comparison.

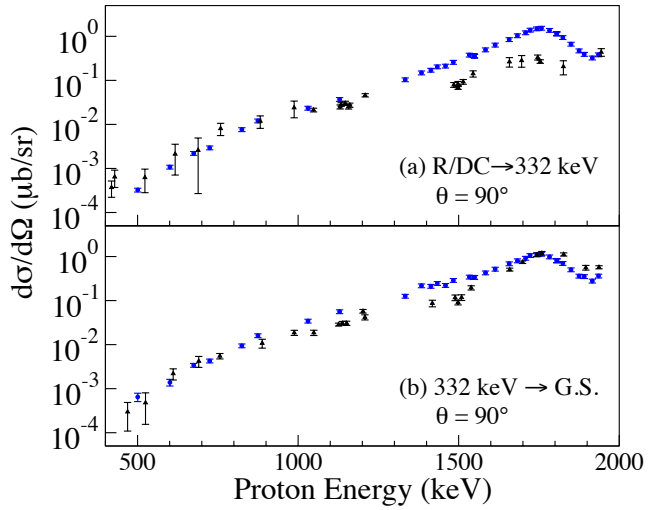

FIG. 11. (Color online) Measured cross sections of the R/DC→332 keV transition, (a), and subsequent decay of the 332 keV state to the ground state,(b), compared to Rolfs *et al.* [7]. Present data are shown as blue circles and Rolfs *et al.* [7] results are black triangles.

The R/DC→332 keV cross section is in agreement with Rolfs *et al.* [7] in the low-energy region, as shown in Fig. 11. However, from E_p = 1.3 - 1.9 MeV, the present cross section is greater than previous measurements. Present results show stronger interference of the $E_{c.m}$ = 1.694 MeV resonance with the non-resonant component than was previously observed. The subsequent first-excited state transition to the ground state

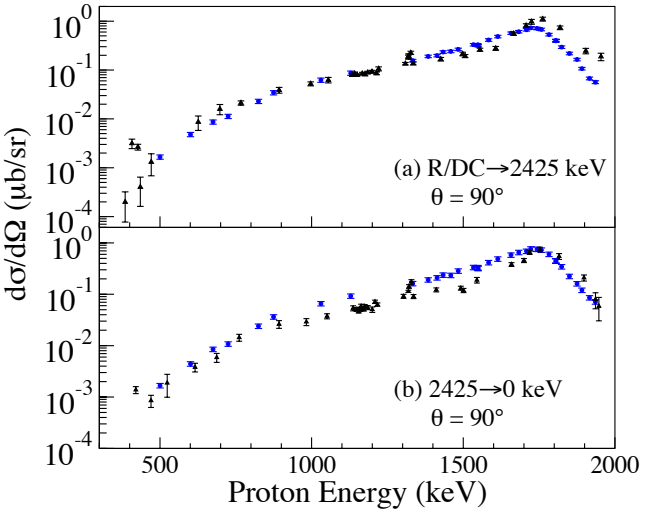

FIG. 12. (Color online) Measured cross sections of R/DC→2425 keV transition, (a), and subsequent decay of the 2425 keV state to the ground state, (b), compared to Rolfs *et al.* [7]. Present data are shown as blue circles and Rolfs *et al.* [7] results are black triangles.

(332 keV→GS) maintains agreement with the previous measurements, except through the mid-energy range, where it is somewhat lower. The 332→0 transition contains increased systematic error, 20%, stemming from a lack of direct efficiency measurements. It should be noted that *R*-Matrix fits to the Rolfs *et al.* [7] data were attempted, but were unable to match the data in this region, as can be seen in Fig. 13.

Fig. 12 shows the R/DC→2425 keV state cross section, which is in agreement with the Rolfs *et al.* [7] cross sections. There is a slight discrepancy in the higher energy region, from E_p = 1.5 - 2.0 MeV. The $E_{c.m}$ = 1.694 MeV (E_x = 4.126 MeV) resonance once again provides significant interference with the non-resonant contribution in the cross section. The present cross section from the 2425 keV to ground state follows a similar trend.

IV. *R*-MATRIX ANALYSIS AND DISCUSSION

A phenomenological *R*-matrix analysis was performed to simultaneously fit the three primary, bound state, γ-ray transitions (ground state, 332, and 2425 keV) of the ^{20}Ne$(p,\gamma)^{21}$Na reaction observed in this work using the code AZURE2 [25]. While secondary transitions were also observed, as shown in Figs. 11 and 12, the *R*-matrix code lacks the capability to properly calculate the differential cross sections for secondary transitions. The model parameters and constants assumed in the analysis are given in Table VI (see below for a discussion of the E_x = 2425 keV state). A simultaneous fitting of scattering data was not possible due to a lack of a reliable data. Currently, only the data of Lambert *et al.* [27] are available, but this work does not present well defined uncertainties and the data requires digitization. As in Rolfs *et al.* [7], no observable yield was detected to the additional bound state in ^{21}Na at 1716 keV. Data in the vicinity of narrow resonances were excluded in the *R*-matrix fits to avoid complications with target effects. For purposes of illustration, these resonances have been included in some of the plots with their level parameters fixed to those in the literature. Neglect of these narrow resonances is permissible since the goal of the *R*-matrix fitting is to model the slowly energy varying portions of the cross section in order to extrapolate to low energy.

TABLE VI. Model parameters and fixed constant parameters of the *R*-matrix analysis. A channel radius of 5.0 fm has been adopted as in Mukhamedzhanov *et al.* [28]. The alternate *R*-matrix parameterization of Brune [29] is used, hence no boundary conditions need to be specified.

Parameter	value	Ref.
a_c	5.0 fm	
M_p	1.00783 amu	[30, 31]
$M_{^{20}\mathrm{Ne}}$	19.99244 amu	[30, 31]
$M_{^{21}\mathrm{Na}}$	20.99765 amu	[30, 31]
S_p	2.43169(14) MeV	[32, 33]
E_{FES}	0.33190(10) MeV	[9]

For modeling the direct capture, the *R*-matrix theory is divided into an internal and external capture part. The external capture is an energy dependent function whose magnitude can be defined by an asymptotic normalization coefficient (ANC) of the bound state [34]. The ANCs can be determined by fitting to capture data but can also be determined by other compound nucleus reaction data like scattering or through transfer reaction measurements. See deBoer *et al.* [35] for a recent description of the general underlying theory.

For the observed transitions of the cross section, all initial parameters for the AZURE2 *R*-matrix analysis had estimates in previous literature. The ANCs were measured in a transfer reaction by Mukhamedzhanov *et al.* [28] and are tabulated together with those obtained here by fitting the capture data in Table VII. Proton widths were taken from Lambert *et al.* [27] and γ-widths from Rolfs *et al.* [7], which are given in Table VIII. The level at E_x = 4.2943 MeV is just above the data for this measurement. While it is included in the analysis at the energy of a real level, the widths can not be interpreted as true widths of this state since their constraint by the data is limited. The level at E_x = 6.0 MeV does not correspond to a real state and is a traditional *R*-matrix background state placed at an arbitrary energy higher than the experimental data. Its proton width has been fixed at the Wigner limit. The cross section of the reaction ^{20}Ne$(p,p_1)^{20}$Ne is negligible over the energy range of the data compared to the elastic scattering cross section. The literature values for these parameters are in good agreement with those found by fitting the present data.

The ANC for the ground state transition subthresh-

old resonance is very sensitive to the level energy as has been highlighted previously [32]. For the energy and uncertainty of the $E_x = 2425$ keV level the adopted value of Iliadis *et al.* [32] ($E_x = 2424.9(4)$ keV) has been taken, which is a weighted average of the measured values of Dubois *et al.* [36] ($E_x = 2423.3(9)$ keV) and of Rolfs *et al.* [7] ($E_x = 2425.2(4)$ keV). For the proton separation energy S_p, the value given in Iliadis *et al.* [32] is also adopted. It is calculated based on the new mass measurements of Mukherjee *et al.* [33]. Variation in the energy of the $E_x = 2425$ keV level and S_p produces a wide range of values for the ANC as given in Table VII. The current capture data and R-matrix analysis find an ANC that is in excellent agreement with that obtained by Mukhamedzhanov *et al.* [28] using ^{20}Ne(^{3}He, d)^{21}Na proton transfer ($7.8(5)\times10^{16}$ fm$^{-1/2}$). It seems that in Mukhamedzhanov *et al.* [28] the energy of the $E_x = 2425$ keV level was not considered in the uncertainty analysis, which accounts for the much larger uncertainty range of the ANC in the present analysis. It should also be noted that to obtain the value of 7.8×10^{16} fm$^{-1/2}$ the excitation energy in the R-matrix analysis had to be tuned carefully to a value of $E_x = 2425$ keV, which is within the adopted range.

The width of the $E_x = 2425$ keV level has been measured previously by Anttila *et al.* [37] who found a value of 0.17(5) eV. The R-matrix fit arrives at an identical value, but the uncertainty analysis indicates a smaller range of 0.17(3) eV. The Breit-Wigner analysis of Rolfs *et al.* [7] on their capture data gives a value of 0.31(7) eV, which is in reasonable agreement.

Only a single unbound level energy, that of the state at $E_x = 4.126$ MeV, is fit in the current analysis (see Table VIII). It corresponds to the only broad resonance in the observed cross section. It appears in each of the different primary transitions and it strongly interferes with the external capture in all of them. The energy of this level does not agree with the value from Rolfs *et al.* [7] of 4.175 ± 0.015 MeV, though is in agreement with previous value from Haas *et al.* [38] of 4.117 ± 0.011 MeV. Additionally, the proton width for the state is larger than that found in the compilation [9]. This state, due to its broad width, has an impact on the S-factor extrapolation at low energy. The γ-widths presented in Table VIII were determined for each observed transition. The direct capture contributions to the cross section are well desecribed by the external capture model. The assumption that $E1$ multipolarity dominates for all the transitions, as proposed by Rolfs *et al.* [7], is consistent with the present data. However, since the differential cross sections of this work were only measured at $\theta_{\rm lab} = 90°$, the amplitudes of other multipole contributions are not well constrained.

The resulting best R-matrix fit is shown in Fig. 13. A good reproduction of the experimental cross sections was obtained for all three primary transitions that were measured. For comparison, the data from Rolfs *et al.* [7] are also shown. The present measurements show interference of the $E_{c.m} = 1.694$ MeV ($E_x = 4.126$ MeV) resonance

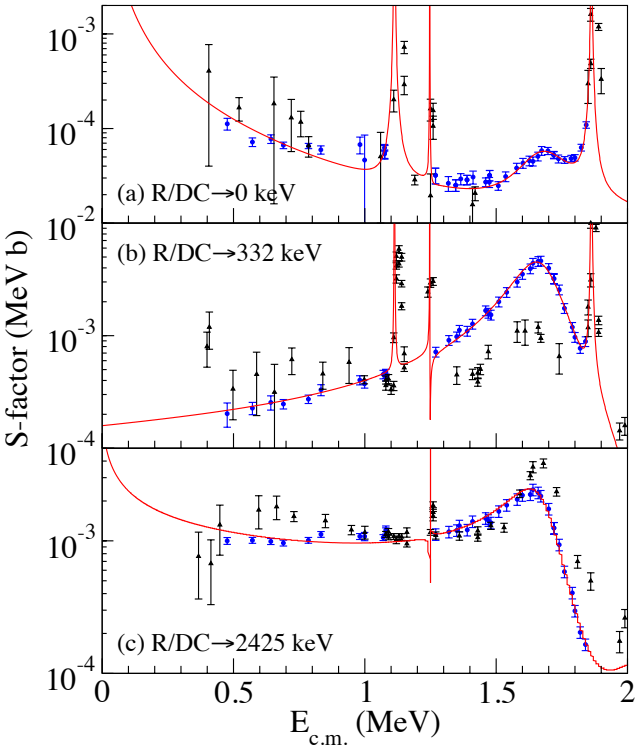

FIG. 13. (Color online) S-factor results from R-matrix fits for all transitions: (a) R/DC→G.S., (b) R/DC→332 keV, (c) R/DC→2425 keV. Present measurements are shown in blue, Rolfs *et al.* [7] are shown in black, and the AZURE2 fits are in red. The fits show good agreement with present results.

in all three transitions. The normalization factors and χ^2 values from the R-matrix fit are given in Table IX. The uncertainties were obtained through a combination of Monte Carlo uncertainty analysis, similar to the one described in deBoer *et al.* [35] and a variation of the energy of the $E_x = 2425$ keV state. In the uncertainty analysis the uncertainty on the ANC that is quoted in Mukhamedzhanov *et al.* [28] is not used. Instead the capture data to the $E_x = 2425$ keV are used to constrain the value of the ANC. Because a variation in the energy of the $E_x = 2425$ keV state is also considered, a much larger uncertainty in the ANC is quoted here than in Mukhamedzhanov *et al.* [28]. However, if the uncertainty in the ANC is calculated for a fixed subthreshold state energy, an uncertainty similar to that of Mukhamedzhanov *et al.* [28] is then obtained. As given in Table VII, the ANCs obtained here for both the 2425 keV state and those of the ground state and 332 keV excited state are consistent with those of Mukhamedzhanov *et al.* [28]. The present analysis yields a value and uncertainty for the zero energy S-factor of 6.3(13) MeV b, very similar to that of Mukhamedzhanov *et al.* [28] of 5.9(12) MeV b.

TABLE VII. Subthreshold state parameters of the R-matrix fit. Note also the energy of the 2425 keV state was changed slightly as discussed in the text, but was fixed at this value in the fitting. The sign on the reduced width corresponds to the interference sign of the reduced width amplitude. **Bold** parameters were varied in the fitting.

Level Energy (keV)		J^π	ANC ($fm^{-1/2}$)		Γ_{γ_0} (eV) (ΠL)	
Present	Refs. [9, 32]		Present	Ref. [28]	Present	Ref. [37]
Bound states						
0	0	$3/2^+$	**0.44(6)**	0.46(4)	–	–
331.9	331.9(1)	$5/2^+$	**-1.6(3)**	1.67(13)	–	–
2424.9[a]	2424.9(4)	$1/2^+$	$\mathbf{-2.80(14)^{+27.2}_{-2.4} \times 10^{17}}$ [b]	$7.8(5)\times10^{16}$	**0.17(3)**	0.17(5) (M1)

[a] The energy was varied over the 1σ range indicated by the adopted value uncertainty.
[b] The uncertainty bounds for the ANC of the $E_x = 2425$ keV state are derived from two sources, that of the Monte Carlo uncertainty analysis that gives a symmetric uncertainty of 0.14×10^{17} $fm^{-1/2}$ and the variation of the energy of the $E_x = 2424.9(4)$ keV and S_p that gives a range of $^{+27.2}_{-2.4} \times 10^{17}$ $fm^{-1/2}$.

TABLE VIII. Parameters of unbound state of the R-matrix fit. **Bold** parameter values were varied in the fitting, all others were fixed to those of the compilation. Minus signs on the partial widths indicate the sign of the corresponding reduced width amplitude. The AZURE2 input file with the best fit parameters of this analysis is given in the Supplemental Material. For further detail, see text.

Level Energy (keV)		J^π	Γ_p (keV)		Γ_{γ_i} (eV) (ΠL)		
Present	Literature [9]		Present	Literature [9]	R/DC →GS	→332	→2425
Unbound state							
4124(5)	4169.6(7)	$3/2^-$	**210(8)**	180(15)	**0.015(2)**(E1)	**-1.1(1)**(E1)	**-0.44(5)**(E1)
Background states							
4294.3	4294.3(6)	$5/2^+$	3.93	3.93(10)	**-0.011(10)**(M1)/**-0.015(11)**(E2)	[a](M1)/**-0.18(5)**(E2)	[a](E2)
6000		$3/2^-$	3500[b]		**0.2(1)**(E1)	**-20(8)**(E1)	**-6.2(11)**(E1)

[a] Consistent with zero.
[b] Fixed at the Wigner limit.

TABLE IX. Normalization factors of the data in the R-matrix fitting. The systematic uncertainty was taken as a common 10%.

Transition (keV)	normalization	N	χ^2
R/DC→0	0.97	34	48.5
R/DC→332	1.10	34	15.2
R/DC→2425	0.95	34	46.3

V. REACTION RATES

The total rate for the ^{20}Ne$(p,\gamma)^{21}$Na reaction was determined using the measured cross sections in combination with previously measured strengths of narrow resonances. The reaction rate is given by

$$N_A\langle\sigma\nu\rangle = N_A\sqrt{\frac{8}{\pi\mu}}(k_BT)^{-3/2}\int_0^\infty \sigma(E)Ee^{\left(-\frac{E}{k_BT}\right)}dE \quad (8)$$

where μ is the reduced mass, $\sigma(E)$ is the cross section, E is center-of-mass energy, and T is the stellar temperature.

AZURE2 was used to calculate the reaction rate contributions by numerical integration of the slowly energy varying components of the S-factor (subthreshold state, external capture, $E_x = 4124$ keV broad resonance, and background levels). The STARLIB reaction rate calculator [39] was used for the narrow resonance contributions. The total rate was then calculated as the sum of these two methods. Other than those noted, the strengths and uncertainties used for the rate contributions from these narrow resonances are the same as those in Iliadis *et al.* [32, 40]. The present reaction rates are given in Table X.

Fig. 14 shows the ratio of each of the components of the reaction rate to the total. The 2425 keV subthreshold state dominates the reaction rate at low temperatures. The R/DC→2425 keV contributes to the reaction rate equally at around $T = 0.07$ GK and dominates the rate at $T = 0.2$ GK. The low-energy narrow resonance at $E_{\rm c.m.} = 366$ keV makes a significant contribution in a limited temperature range near 0.5 GK, while the weaker $E_{\rm c.m.} = 397$ keV resonance has a limited effect on the rate. The $E_{\rm c.m.} = 1113$ keV resonance becomes the dominant component around $T = 2$ GK and the new resonance strength results in a slight reduction in the rate for this resonant component. The direct capture dominated 332 keV transition has a small effect throughout most of the temperature region of interest, finally becoming the dominant contribution at the highest temperatures investigated.

The reaction rates were compared to those in NACRE [8] and Iliadis *et al.* [40], as shown in Fig. 15. For the comparison, the present rates and those from Iliadis *et al.* [40]

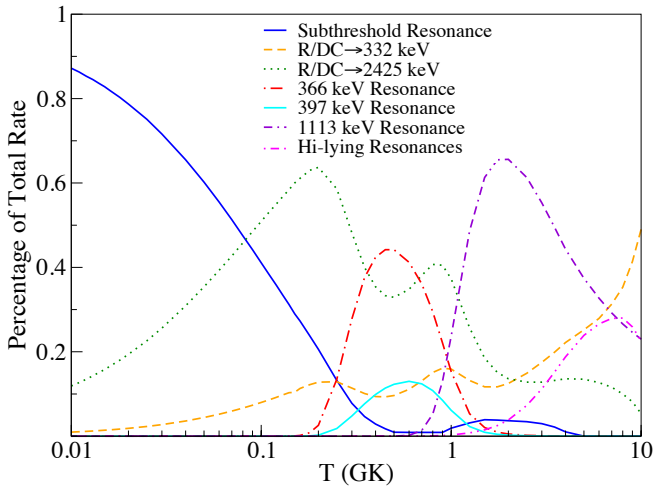

FIG. 14. (Color online) Ratio of the various reaction components rates to the total rate determined as a function of the temperature in GK. The various colors represent each component. The contribution from high-lying resonances was summed together.

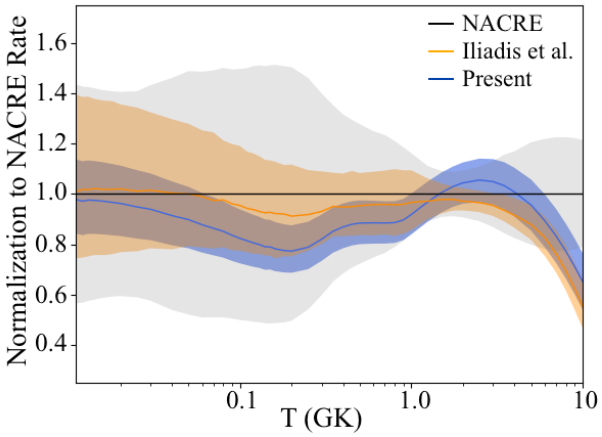

FIG. 15. (Color online) Ratio of the present total reaction rate and that given in Iliadis *et al.* [40] compared to that of NACRE [8], including respective error bands. The ratio of the present reaction rate is shown in blue, Iliadis *et al.* [40] is shown in orange, and NACRE is in grey.

were divided by the NACRE adopted rate. The present total rate is lower by roughly 20% in some regions compared to Iliadis *et al.* [40] and NACRE. This is because both Iliadis *et al.* [40] and NACRE use the S-factor from Rolfs *et al.* [7], which is much higher than that obtained in the present work due to the uncertainties in the subthreshold resonance. As previously discussed IV, this is likely due to a gamma width that is roughly two-times larger than presently determined. The present reaction rate follows the trend of Iliadis *et al.* [40] at higher energies.

VI. SUMMARY AND CONCLUSION

The excitation functions for the ^{20}Ne$(p,\gamma)^{21}$Na reaction have been measured over the energy range $E_p = 500$ - 2000 keV relative to the $E_{\rm c.m.} = 1113$ keV resonance. The resonance strength of the $E_{\rm c.m.} = 1113$ keV resonance has been independently determined for this work and is in agreement with previous literature values [10, 17]. The cross sections were determined for the various direct capture transitions in the energy range measured, improving upon previous measurements [7]. Significant interference effects from the $E_{c.m} = 1.742$ MeV resonance were observed from each transition. Most notably this was the first observation of this interference in the R/DC→0 transition. The cross sections were analyzed using R-matrix code AZURE2 to extrapolate the astrophysical S-factor to lower energies [25]. In the analysis all primary transitions were fit simultaneously along with previous data from Rolfs *et al.* [7]. It was found that the energy of the subthreshold state greatly impacted the ANC value required to achieve the best fit. Variations as small as 0.7 keV could impact the ANC value by orders of magnitude. The parameters used in the best fit were in agreement with literature values [7, 27, 28]. An AZURE2 file with the best fit is included in the Supplemental Material [41].

The reaction rate determined from the R-matrix analysis is lower, by up to 20%, than the rates in various rate libraries [8, 39], though still in agreement within the respective uncertainties. It was determined that the R/DC→0 component of the reaction rate is negligible at astrophysically relevant temperature, which is dominated by the subthreshold state.

As a next step to improve the uncertainty of the reaction rate, more confident measurements of the lifetime and ANC of the $E_x = 2425$ keV subthreshold state should be made. Additionally, scattering data with well defined uncertainties would provide additional constraint. Further measurements of the capture cross section below $E_p = 500$ keV are possible, but would be challenging.

VII. ACKNOWLEDGMENTS

This research utilized resources from the Notre Dame Center for Research Computing and was supported by the National Science Foundation through Grant No. Phys-0758100, and the Joint Institute for Nuclear Astrophysics through Grant No. Phys-0822648 and PHY-1430152 (JINA Center for the Evolution of the Elements). S. Lyons was supported by the DOE NNSA Stewardship Science Graduate Fellowship (DE-FC52-08NA28752).

TABLE X. Reaction rates determined from present cross section measurements. Rates were calculated using AZURE2 and STARLIB rate calculator.

T (GK)	Low Rate	Median Rate	High Rate
0.010	6.33×10^{-29}	7.33×10^{-29}	8.51×10^{-29}
0.011	9.14×10^{-28}	1.06×10^{-27}	1.23×10^{-27}
0.012	9.67×10^{-27}	1.12×10^{-26}	1.29×10^{-26}
0.013	7.95×10^{-26}	9.18×10^{-26}	1.06×10^{-25}
0.014	5.31×10^{-25}	6.12×10^{-25}	7.08×10^{-25}
0.015	2.97×10^{-24}	3.43×10^{-24}	3.96×10^{-24}
0.016	1.43×10^{-23}	1.65×10^{-23}	1.91×10^{-23}
0.018	2.31×10^{-22}	2.66×10^{-22}	3.06×10^{-22}
0.020	2.52×10^{-21}	2.90×10^{-21}	3.33×10^{-21}
0.025	2.99×10^{-19}	3.43×10^{-19}	3.92×10^{-19}
0.030	1.13×10^{-17}	1.29×10^{-17}	1.47×10^{-17}
0.040	2.19×10^{-15}	2.49×10^{-15}	2.82×10^{-15}
0.050	9.16×10^{-14}	1.03×10^{-13}	1.17×10^{-13}
0.060	1.56×10^{-12}	1.76×10^{-12}	1.98×10^{-12}
0.070	1.50×10^{-11}	1.68×10^{-11}	1.88×10^{-11}
0.080	9.61×10^{-11}	1.07×10^{-10}	1.20×10^{-10}
0.090	4.62×10^{-10}	5.14×10^{-10}	5.74×10^{-10}
0.100	1.78×10^{-09}	1.98×10^{-09}	2.20×10^{-09}
0.110	5.79×10^{-09}	6.41×10^{-09}	7.13×10^{-09}
0.120	1.64×10^{-08}	1.81×10^{-08}	2.01×10^{-08}
0.130	4.16×10^{-08}	4.59×10^{-08}	5.09×10^{-08}
0.140	9.62×10^{-08}	1.06×10^{-07}	1.17×10^{-07}
0.150	2.15×10^{-07}	2.36×10^{-07}	2.62×10^{-07}
0.160	4.14×10^{-07}	4.54×10^{-07}	5.02×10^{-07}
0.180	1.42×10^{-06}	1.56×10^{-06}	1.72×10^{-06}
0.200	4.18×10^{-06}	4.57×10^{-06}	5.04×10^{-06}
0.250	3.97×10^{-05}	4.34×10^{-05}	4.77×10^{-05}
0.300	2.50×10^{-04}	2.72×10^{-04}	2.99×10^{-04}
0.350	1.11×10^{-03}	1.21×10^{-03}	1.32×10^{-03}
0.400	3.67×10^{-03}	4.00×10^{-03}	4.37×10^{-03}
0.450	9.60×10^{-03}	1.05×10^{-02}	1.14×10^{-02}
0.500	2.11×10^{-02}	2.30×10^{-02}	2.50×10^{-02}
0.600	7.10×10^{-02}	7.73×10^{-02}	8.40×10^{-02}
0.700	1.77×10^{-01}	1.93×10^{-01}	2.09×10^{-01}
0.800	3.80×10^{-01}	4.13×10^{-01}	4.48×10^{-01}
0.900	7.67×10^{-01}	8.32×10^{-01}	9.01×10^{-01}
1.000	$1.52 \times 10^{+00}$	$1.64 \times 10^{+00}$	$1.78 \times 10^{+00}$
1.250	$7.30 \times 10^{+00}$	$7.92 \times 10^{+00}$	$8.55 \times 10^{+00}$
1.500	$2.55 \times 10^{+01}$	$2.76 \times 10^{+01}$	$2.98 \times 10^{+01}$
1.750	$6.55 \times 10^{+01}$	$7.11 \times 10^{+01}$	$7.67 \times 10^{+01}$
2.000	$1.34 \times 10^{+02}$	$1.46 \times 10^{+02}$	$1.58 \times 10^{+02}$
2.500	$3.67 \times 10^{+02}$	$4.02 \times 10^{+02}$	$4.36 \times 10^{+02}$
3.000	$7.14 \times 10^{+02}$	$7.86 \times 10^{+02}$	$8.55 \times 10^{+02}$
3.500	$1.14 \times 10^{+03}$	$1.26 \times 10^{+03}$	$1.38 \times 10^{+03}$
4.000	$1.61 \times 10^{+03}$	$1.78 \times 10^{+03}$	$1.95 \times 10^{+03}$
5.000	$2.56 \times 10^{+03}$	$2.85 \times 10^{+03}$	$3.14 \times 10^{+03}$
6.000	$3.41 \times 10^{+03}$	$3.81 \times 10^{+03}$	$4.21 \times 10^{+03}$
7.000	$4.11 \times 10^{+03}$	$4.60 \times 10^{+03}$	$5.09 \times 10^{+03}$
8.000	$4.65 \times 10^{+03}$	$5.21 \times 10^{+03}$	$5.78 \times 10^{+03}$
9.000	$5.04 \times 10^{+03}$	$5.66 \times 10^{+03}$	$6.28 \times 10^{+03}$
10.00	$5.31 \times 10^{+03}$	$5.97 \times 10^{+03}$	$6.63 \times 10^{+03}$

[1] J. B. Marion and W. A. Fowler, The Astrophysical Journal **125**, 221 (1957).
[2] R. M. Cavallo, A. V. Sweigart, and R. A. Bell, The Astrophysical Journal Letters **464**, L79 (1996).
[3] R. M. Cavallo, A. V. Sweigart, and R. A. Bell, The Astrophysical Journal **492**, 575 (1998).
[4] T. Matheson, A. V. Filippenko, and L. C. Ho, The Astrophysical Journal **418**, L29 (1993).
[5] C. Iliadis, J. M. D'Auria, S. Starrfield, W. J. Thompson, and M. Wiescher, The Astrophysical Journal Supplement Series **134**, 151 (2001).
[6] M. F. El Eid, B. S. Meyer, *et al.*, The Astrophysical Journal **655**, 1058 (2007).
[7] C. Rolfs, W. Rodne, M. Shapiro, and H. Winkler, Nuclear Physics A **241**, 460 (1975).
[8] C. Angulo, M. Arnould, and M. Rayet, Nucl. Phys. A **656** (1999), https://doi.org/10.1016/S0375-9474(99)00030-5.
[9] R. Firestone, Nuclear Data Sheets **127**, 1 (2015).
[10] G. Thomas and N. Tanner, Proceedings of the Physical Society **75**, 498 (1960).
[11] W. A. Fowler, C. C. Lauritsen, and T. Lauritsen, Rev. Mod. Phys. **20**, 236 (1948).
[12] M. Meyer, I. Venter, and D. Reitmann, Nuclear Physics A **250**, 235 (1975).
[13] A. Antilla, J. Keinonen, M. Hautala, and I. Forsblom, Nuclear Instruments and Methods **147**, 501 (1977).
[14] G. F. Knoll, *Radiation Detection and Measurement* (John Wiley & Sons, 2010).
[15] Geant Collaboration, Nuclear Instruments and Methods in Physics Research Section A: Accelerators, Spectrometers, Detectors and Associated Equipment **506**, 250 (2003).
[16] K. Debertin and U. Schötzig, Nuclear Instruments and Methods **158**, 471 (1979).
[17] G. Christian, D. Hutcheon, C. Akers, D. Connolly, J. Fallis, and C. Ruiz, Physical Review C **88**, 038801 (2013).
[18] J. Keinonen, M. Riihonen, and A. Anttila, Physical Review C **15**, 579 (1977).
[19] S. Engel, D. Hutcheon, S. Bishop, L. Buchmann, J. Caggiano, M. Chatterjee, A. Chen, J. D?Auria, D. Gigliotti, U. Greife, *et al.*, Nuclear Instruments and Methods in Physics Research Section A: Accelerators, Spectrometers, Detectors and Associated Equipment **553**, 491 (2005).
[20] W. Hammer, W. Biermayer, T. Griegel, H. Knee, and K. Petkau, (1999), unpublished.
[21] R. Bloch, T. Knellwolf, and R. Pixley, Nuclear Physics A **123**, 129 (1969).
[22] C. Van der Leun and W. Mouton, Physica **30**, 333 (1964).
[23] C. Dunford and T. Burrows, "Online nuclear data service," Report **IAEA-NDS-150** (NNDC Informal Report **NNDC/ONL-95/10**), International Atomic Energy Agency, vienna, Austria.
[24] M. Rose, Physical Review **91**, 610 (1953).
[25] R. Azuma, E. Uberseder, E. Simpson, C. Brune, H. Costantini, R. De Boer, J. Görres, M. Heil, P. LeBlanc, C. Ugalde, *et al.*, Physical Review C **81**, 045805 (2010).
[26] E. Stech, *The Astrophysical Impact of the* $^{20}Ne(p,\gamma)^{21}Na$ *Reaction*, Ph.D. thesis, University of Notre Dame (2004).
[27] M. Lambert, P. Midy, D. Drain, M. Amiel, H. Beaumevieille, A. Dauchy, and C. Meynadier, Journal de Physique **33**, 155 (1972).
[28] A. Mukhamedzhanov, P. Bém, V. Burjan, C. Gagliardi, B. Irgaziev, V. Kroha, J. Novák, Š. Piskoř, E. Šimečková, R. Tribble, *et al.*, Physical Review C **73**, 035806 (2006).
[29] C. R. Brune, Phys. Rev. C **66**, 044611 (2002).
[30] W. Huang, G. Audi, M. Wang, F. Kondev, S. Naimi, and X. Xu, Chinese Physics C **41**, 030002 (2017).
[31] M. Wang, G. Audi, F. Kondev, W. Huang, S. Naimi, and X. Xu, Chinese Physics C **41**, 030003 (2017).
[32] C. Iliadis, R. Longland, A. E. Champagne, A. Coc, and R. Fitzgerald, Nuclear Physics A **841**, 31 (2010).
[33] M. Mukherjee, A. Kellerbauer, D. Beck, K. Blaum, G. Bollen, F. Carrel, P. Delahaye, J. Dilling, S. George, C. Guénaut, F. Herfurth, A. Herlert, H.-J. Kluge, U. Köster, D. Lunney, S. Schwarz, L. Schweikhard, and C. Yazidjian, Phys. Rev. Lett. **93**, 150801 (2004).
[34] A. M. Mukhamedzhanov, C. A. Gagliardi, and R. E. Tribble, Phys. Rev. C **63**, 024612 (2001).
[35] R. J. deBoer, J. Görres, M. Wiescher, R. E. Azuma, A. Best, C. R. Brune, C. E. Fields, S. Jones, M. Pignatari, D. Sayre, K. Smith, F. X. Timmes, and E. Uberseder, Rev. Mod. Phys. **89**, 035007 (2017).
[36] J. Dubois, H. Odelius, and S. O. Berglund, Physica Scripta **5**, 163 (1972).
[37] A. Anttila, J. Keinonen, and M. Bister, Journal of Physics G: Nuclear Physics **3**, 1241 (1977).
[38] F. Haas, C. Johnson, and J. Bair, Nuclear Physics A **193**, 65 (1972).
[39] A. L. Sallaska, C. Iliadis, A. Champange, S. Goriely, S. Starrfield, and F. Timmes, The Astrophysical Journal Supplement Series **207**, 18 (2013).
[40] C. Iliadis, R. Longland, A. E. Champagne, and A. Coc, Nuclear Physics A **841**, 251 (2010).
[41] See Supplemental Material at [URL from publisher] for AZURE2 file with fit parameters from this work. The differential cross section data for the three direct capture transitions is also available as input data. To use these files, one will need to have AZURE2 installed, which is available at azure.nd.edu.